Mutational and structural analysis of an ancestral fungal dye-decolorizing peroxidase

Ulises A. Zitare[1,2], Mohamed H. Habib[1,3] (iD), Henriette Rozeboom[1], Maria L. Mascotti[1,4], Smilja Todorovic[5] and Marco W. Fraaije[1] (iD)

1 Molecular Enzymology Group, University of Groningen, The Netherlands
2 Instituto de Química Física de los Materiales, Medio Ambiente y Energía (INQUIMAE), Departamento de Química Inorgánica, Analítica y Química Física, Facultad de Ciencias Exactas y Naturales, Universidad de Buenos Aires and CONICET, Argentina
3 Department of Microbiology and Immunology, Faculty of Pharmacy, Cairo University, Egypt
4 IMIBIO-SL CONICET, Facultad de Química Bioquímica y Farmacia, Universidad Nacional de San Luis, Argentina
5 Instituto de Tecnologia Química e Biológica, Universidade Nova de Lisboa, Oeiras, Portugal

Dye-decolorizing peroxidases (DyPs) constitute a superfamily of heme-containing peroxidases that are related neither to animal nor to plant peroxidase families. These are divided into four classes (types A, B, C, and D) based on sequence features. The active site of DyPs contains two highly conserved distal ligands, an aspartate and an arginine, the roles of which are still controversial. These ligands have mainly been studied in class A-C bacterial DyPs, largely because no effective recombinant expression systems have been developed for the fungal (D-type) DyPs. In this work, we employ ancestral sequence reconstruction (ASR) to resurrect a D-type DyP ancestor, AncDyPD-b1. Expression of AncDyPD-b1 in *Escherichia coli* results in large amounts of a heme-containing soluble protein and allows for the first mutagenesis study on the two distal ligands of a fungal DyP. UV-Vis and resonance Raman (RR) spectroscopic analyses, in combination with steady-state kinetics and the crystal structure, reveal fine pH-dependent details about the heme active site structure and show that both the aspartate (D222) and the arginine (R390) are crucial for hydrogen peroxide reduction. Moreover, the data indicate that these two residues play important but mechanistically different roles on the intraprotein long-range electron transfer process.

Database
Structural data are available in the PDB database under the accession number 7ANV.

Introduction

Dye-decolorizing peroxidases (DyPs) constitute a superfamily of heme-containing peroxidases found in bacteria, fungi, and some archaea [1]. Since the first report in 1999 [2], there has been a growing interest in DyPs, partly due to their conspicuous catalytic properties [3]. Namely, different DyPs have shown the ability to oxidize a wide range of structurally distinct and complex substrates including azo dyes, anthraquinones, lignin-related compounds, and even alkenes [2,4–6].

DyP-type peroxidases have been classified according to two main clustering criteria: (a) into four types, A,

B, C, and D based on sequence similarity and their overall topology [7]; and (b) more recently into three main types, P (primitive), I (intermediate), and V (advanced) [8]. In the former, type A DyPs are defined by the presence of a Tat-dependent signal sequence enabling them to function outside the cytoplasm. In addition, they have amino acid sequences shorter than those of types D and C but longer than type B DyPs. Some of the type A proteins are components of tripartite ferrous iron transporters [8]. Notably, B- and C-type DyPs are putative cytoplasmic enzymes, suggesting that they play a role in intracellular metabolism. Type B proteins have the shortest amino acid sequence among all, and in some cases, the respective encoding genes constitute an operon [9]. Type C DyPs are the least studied and represented in literature. They are structurally closer to the type D DyPs, but they typically lack the N-terminal pro-sequence, usually found in the latter [8]. Finally, the type D DyPs are exclusively found in fungi [10]. A unique feature of these enzymes is that the N-terminal amino acids are cleaved in some of its members, which could be correlated with the processing of the N-terminal pro-sequence during maturation. Owing to the low degree of similarity among the different types (A, B, C, and D), inaccurate multiple sequence alignments and estimates of evolutionary relationships have emerged [8]. This led Yoshida and Sugano to propose a different classification, where the former type B DyPs are named type P, as the sequences in this class are more compact. The newly proposed type V DyPs contain C- and D-type enzymes due to the presence of similar amino acid sequences in the same regions, which makes it sometimes difficult to differentiate between the two types phylogenetically. Type I represents the former type A enzymes, as this class has a few extra sequences than the class V. In order to facilitate the discussion and owing to the fact that the type D DyP, which, unlike C-type DyPs, has fungal origin, is in the focus of this article, we will refer to the firstly proposed classification throughout this work.

The four DyP types originate from a common family, and representatives from classes A, B, C, and D show similar tertiary structures [8]. However, they do not share any sequence or structural features with the archetypal animal and plant peroxidase families. For instance, while classical plant peroxidase structure is mainly composed of α-helices [11], the overall structure of DyPs harbors a ferredoxin-like fold and is rich in both α-helices and β-sheets [12,13]. Both families share a similar active site structure, with a proximal histidine as a strong ligand of the iron, and an arginine in the distal heme cavity, [1] but the distal histidine, essential for the plant peroxidases, is absent in DyPs. Instead, there is a conserved aspartate, substituted by a glutamate in some rare cases, which is part of the DyP-typifying sequence fingerprint motif GXXDG [1,14,15]. The role of both aspartate and arginine is unclear, but it has been proposed that the aspartate takes up the crucial catalytic role of the distal histidine of plant peroxidases. This hypothesis was supported with studies on DyP mutants in which the aspartate had been replaced resulting in very low to no peroxidase activity [14,16]. Nevertheless, there are reports where such mutation only had a minor effect on activity [17,18]. Similarly, mutating the distal arginine resulted in an inconsistent impact on enzyme activity. It is worth noting, however, that almost all mutagenesis studies on DyPs were performed on A-type [17,19–21] and B-type [18,22,23] DyPs. Reports on engineering of a D-type DyP are scarce [16,24].

Type D DyPs are exclusively found in dikarya fungi [8] and have typically been studied by isolation from their native species. Such purification procedures are typically laborious and result in relatively low yields when compared with recombinantly expressed proteins. On the other hand, the expression of fungal peroxidases in bacterial hosts can be challenging, as it is the case of other eukaryotic heme-containing peroxidases [25]. For example, Behrens *et al.* [26] reported the expression of four fungal DyPs in *E. coli* by using a cold-shock-inducible expression system. Nevertheless, the lack of a reliable recombinant expression system for D-type DyPs has hindered the study of this particular group of enzymes. An unexplored strategy until date is to perform ancestral sequence reconstruction (ASR), which could yield a variant suitable as prototype D-type DyP and furthermore reveal features related to the evolution of these enzymes. ASR was first proposed by Pauling and Zuckerkandl in 1963 when they showed that modern proteins contain enough information to resurrect ancient protein sequences [27]. This so-called vertical approach consists in obtaining the sequence of extant proteins by means of phylogenetic inference [28]. Ancestral enzymes are then obtained and experimentally characterized [29]. ASR has allowed to resurrect functional ancient proteins from the Precambrian period as well as to trace evolutionary events that have led extant proteins to acquire their current functional and structural features [30]. In particular, several peroxidase ancestors have been characterized [31,32], which demonstrate the power of ASR in understanding the biochemistry and functionality of these enzymes. However, no ASR of DyPs has been performed so far.

In this work, we resurrected a D-type DyP from a basidiomycetes group, AncDyPD-b1, and overexpressed it as a soluble, heme-containing, and active protein in *E. coli*. We performed a site-directed mutagenesis study on the aspartate and the arginine at the active site, providing new insights into the role of these residues. Spectroscopic analysis allowed us to rationalize the pH-dependent catalytic activity toward various substrates, while elucidation of the crystal structure of AncDyPD-b1 provided a detailed view on its active site.

Results and Discussion

Ancestral sequence reconstruction of a D-type DyP from a basidiomycetes group

An exhaustive phylogenetic analysis of the whole DyPs family, which aimed at discriminating among sequences from different types, was performed employing a representative and nonredundant dataset (Fig. 1). Sequences from the different DyP types were identified, and the observed clustering was in agreement with previous reports [8]. The C- and D-type DyPs formed a clade, supporting the new classification proposed by Yoshida and Sugano in 2015. The fungal origin was identified as the distinctive feature of the D-type DyPs.
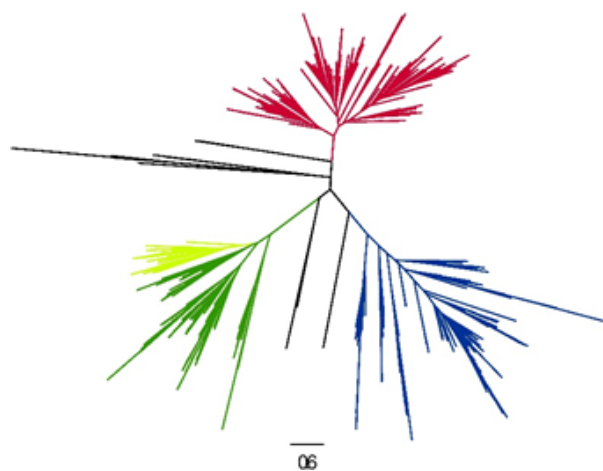
The taxonomic distribution among D-type DyPs reveals only species belonging to the dikarya subkingdom lineages (Basidiomycetes and Ascomycetes phyla). Interestingly, sequences from basidiomycetes form a clade, while those from ascomycetes do not (Fig. 2). All experimentally characterized fungal DyPs so far belong to basidiomycete species. The topology of the tree shows that D-type DyPs are distributed into two subgroups. One of them includes most of the known sequences, such as *Aau*DyPI from *Auricularia auricula–judae* [33] and *Bad*DyP from *Bjerkandera adusta* [14]. The other subgroup is formed by mostly unknown sequences and *Ftr*DyP from *Funalia (Coriolopsis) trogii* [34] and *Gl*DyP from *Ganoderma lucidum* [35].

In order to get a more accurate understanding of the D-type DyPs biochemistry, ancestral sequence reconstruction (ASR) was performed. The nodes for two of the groups of *basidiomycota* sequences were selected for experimental characterization (Fig. 2). These ancestors, named AncDyPD-b1 and AncDyPD-b2, were reconstructed with overall posterior probabilities (PP) of 0.85 and 0.76, respectively (Data S3). AncDyPD-b1 was obtained as a recombinant enzyme and analyzed in more detail, while AncDyPD-b2 could not be expressed. Among the 511 sites in AncDyPD-b1, 88 were ambiguously reconstructed, showing alternative states with PP > 0.2. Most of the ambiguously reconstructed residues are on the surface of the protein (Fig. S1), and 35% correspond to conservative changes. To assess the robustness of our reconstruction, the alternative ancestor (AncAltDyPD-b1) was also obtained and subsequently characterized. AncDyPD-b1 shows 61% sequence identity with *Pos*-DyP4 from *Pleurotus ostreatus* (Q0VTU1) and 50% identity with *Bad*DyP from *Bjerkandra adusta* (Q8WZK8) and *Aau*DyPI (I2DBY1) (Fig. S2).

Expression and purification

AncDyPD-b1, AncAltDyPD-b1, and AncDyPD-b2 encoding genes were cloned in pBAD plasmids for expression as His-tagged SUMO-fused recombinant proteins. Expression of AncDyPD-b2 was found to be challenging, and no soluble enzyme could be obtained. Expression and purification of AncDyPD-b1 and AncAltDyPD-b1 resulted in red-brownish protein samples. SDS/PAGE analysis of the purified enzymes indicated a molecular mass of 69 kDa, which is in full agreement with the 68 992 Da and 68 735 Da predicted sizes of the SUMO-fused AncDyPD-b1 and AncAltDyPD-b1, respectively. Several alternative *E. coli* strains were tested (BL21 DE3, BL21 DE3*,

Fig. 1. Phylogenetic tree of DyPs. The tree was constructed by the ML method in PHYML 3.0 using a representative and nonredundant dataset (MSA included 641 sequences, 563 sites). Colored groups include experimentally characterized DyPs: A type (red), B type (blue), and C+D type (green). The D DyP subclade is highlighted in light green.
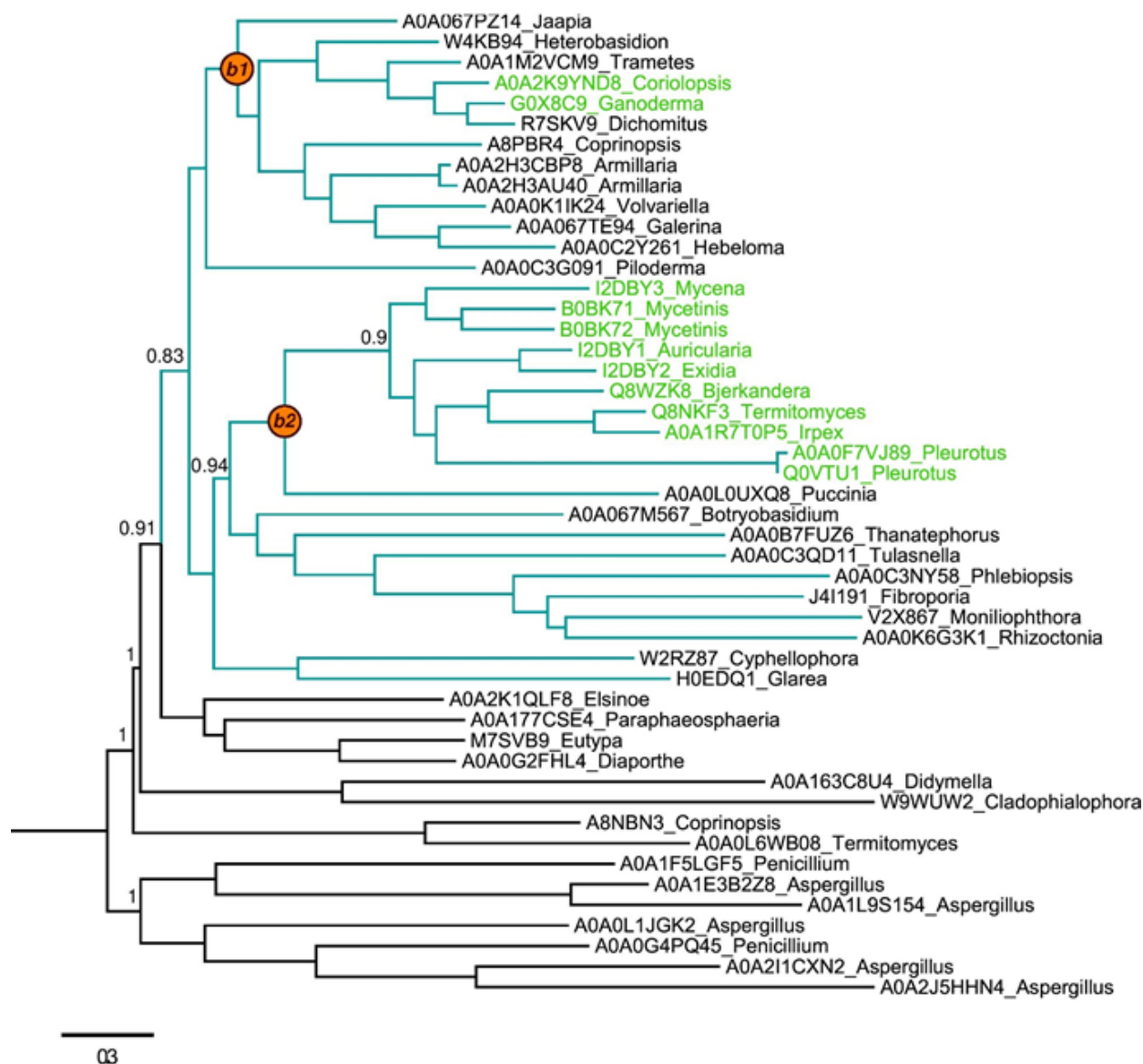
Fig. 2. Phylogeny of D-type DyPs. Tree was constructed in PHYML 3.0, and 500 BS were run and subjected to bootstrap transfer. TBE values of major divergences are shown at the nodes. UniProt accession code and genus is given for each sequence. *Ascomycota* sequences are shown in black branches and *basidiomycota* in teal branches. Experimentally characterized enzymes are written in green. The ancestors selected for experimental characterization, AncDyPD-b1 and AncDyPD-b2, are marked with orange circles.

BL21 AI, and C41) for expression. Only *E. coli* BL21 AI and *E. coli* NEB 10β showed successful expression of soluble AncDyPD-b1. Without extensive optimization of the expression conditions, up to 140 mg of purified SUMO-AncDyPD-b1 per liter of culture broth was obtained using *E. coli* NEB 10β cells. Treatment of SUMO-constructs with SUMO protease allowed purification of untagged enzymes.

We designed, expressed, and purified five variants of one or both distal ligands, that is, D222 and R390,

employing a standard QuikChange procedure. Remarkably, both sites were reconstructed with PPs = 1 in AncDyPD-b1. The strategy was to design one conservative (D→E, R→K) and one nonconservative (D→A, R→A) variant of both residues and a variant that combines both conservative modifications. Given the strong disruptive effect of nonconservative variations on enzyme activity and stability (*vide infra*), double variants containing such mutations were not assessed. The five AncDyPD-b1 variants (D222E,

D222A, R390K, R390A, and D222E/R390K) were expressed and purified following the same protocol as wild-type (WT) AncDyPD-b1.

Heme active site, enzymatic activity, thermostability, and effect of pH

The absorbance spectrum of AncDyPD-b1 WT reveals a Soret band at 426 nm, a lower intensity but significant band at 360 nm and two partially superimposed and relatively broad bands in the Q region at 545 and 575 nm (Fig. 3A). The UV-Vis spectrum of AncAlt-DyPD-b1 is indistinguishable from AncDyPD-b1, and spectra after SUMO cleavage were identical in both cases. This indicates that neither the SUMO domain nor the amino acids that vary between AncDyPD-b1 and AncAltDyPD-b1 have any impact on the heme electronic structure. The position of the Soret band is significantly upshifted in comparison with the usually reported values for ferric hemes (around 410 nm). Interestingly, it shows a shoulder at approximately 410 nm, which may suggest that the enzyme is in an

equilibrium between two states. In order to assess the redox activity and ligand-binding properties of the heme iron, we evaluated UV-Vis spectra upon addition of hydrogen peroxide, sodium dithionite, imidazole, azide, nickel chloride, and manganese sulfate. The additions were up to 1 mM, employing both 50 and 500 μM of protein. However, there was no significant spectroscopic change observed upon addition of any of these molecules. Further studies are necessary to clarify the unusual absorbance features of the WT AncDyPD-b1 and its alternative counterpart, WT AncAltDyPD-b1.

UV-Vis spectra of all variants present similar absorbance features, that is, a strong Soret band, a lower intensity band at lower wavelength, and two partially superimposed Q bands (Fig. 3B). A closer inspection shows that for the R390A, D222E and D222E-R390K variants the Soret bands are broadened and blue-shifted (409, 413, and 414 nm, respectively) to values similar to those of regular heme-containing proteins. On the other hand, the Soret bands of R390K and D222A variants at 423 and 425 nm, respectively, are almost identical to the WT. These results show that both residues participate in the fine-tuning of the AncDyPD-b1 cofactor electronic structure.

Heme incorporation of the variants relative to the WT AncDyPD-b1 was estimated by comparing A_{Soret}/A_{280} ratios, which revealed 3%, 33%, 100%, 70%, and 10% heme incorporation for R390A, R390K, D222A, D222E, and D222E-R390K, respectively. Notably, heme incorporation in the aspartate mutant D222A was slightly affected, while that of D222E was unaffected. Mutant proteins harboring an arginine mutation suffered from poor heme incorporation. Indeed, it was observed that the latter mutant proteins showed lower stability (*vide infra*). These results suggest a structural role of the distal arginine in stabilizing the heme/protein matrix interactions.

The peroxidase activity of AncDyPD-b1 and the alternative ancestor was tested using ABTS, RB5, DB71, and RB19. All the substrates were oxidized at low pH (between 3.0 and 4.0) and in the presence of H_2O_2, while there was no significant activity at pH 7.0. This shows that the reconstructed DyP is catalytically competent and displays substrate promiscuity with a low optimum pH, which is typical for DyPs [4,8,10]. Oxidation of ABTS and RB5 was also tested after SUMO cleavage, and no differences were found. Interestingly, AncDyPD-b1 and AncAltDyPD-b1 also showed the capability to oxidize Mn^{+2}. This feature is shared by other DyPs and has been speculated as important for microbial lignin degradation [36]. In addition, peroxygenase activity, first reported for
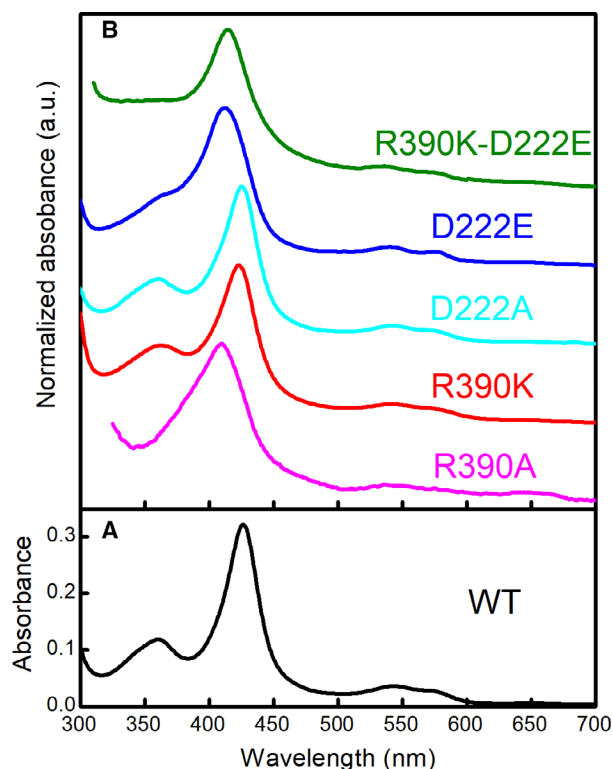

Fig. 3. (A) UV-Vis spectrum of AncDyPD-b1 WT 0.01 M. (B) Normalized UV-Vis spectra of AncDyPD-b1 (pink) R390A, (red) R390K, (cyan) D222A, (blue) D222E, and (green) R390K-D222E. All spectra were recorded at 25 °C using a 50 mM potassium phosphate buffer pH 7.5 containing 150 mM NaCl and 10% v/v glycerol.

*Tfu*DyP [37], was also tested. However, no conversion of thioanisole by AncDyPD-b1 was detected at 17, 25, and 30 °C (Data S4).

The thermostability of AncDyPD-b1 and AncAlt-DyPD-b1 was assessed by measuring UV-Vis spectra and peroxidase activity using ABTS as a substrate after incubation at different temperatures (Table S2). There were no significant spectral changes in any case. The relative remaining activity values suggest that this ancestor has a slightly lower stability when compared to the biochemically characterized descendant *Ftr*DyP [34]. In that case, a 60% activity loss is observed after 1-h incubation at 40 °C. The stability of protein variants upon one-hour incubation at 20 °C was also tested. The aspartate variants showed similar results to WT AncDyPD-b1, while arginine variants revealed a complete loss of activity even after 30-min incubation. This result reinforces the suggestion that the distal arginine ligand plays a structural role, facilitating heme binding and stability within the protein.

In order to investigate the effect of pH on the heme electronic structure, UV-Vis spectra of WT AncDyPD-b1 and its variants were recorded at different pH values (Fig. 4). WT AncDyPD-b1, D222A, and D222E showed a transition below pH 4.0 characterized by a loss of the Soret and Q band intensities and a rise of a broad and asymmetrical band around 370 nm (Fig. 4A,C,D). A similar transition was observed in both R390K containing variants below pH 6.0 (Fig. 4B,E). The changes observed at low pH are fully reversible and take place in the time scale of minutes (Fig. S3). In addition, a subtle transition is observed between pH 5.0 and pH 6.0 in every variant. It consists of a slight red-shift of the Soret band, most likely due to a protonation change close to the heme, which, however, does not affect the iron coordination (*vide infra*). Interestingly, optimum values for the oxidation of ABTS and RB5 were found to be pH 3.0 and pH 4.0, respectively, for every AncDyPD-b1 variant (Fig. S4), suggesting that a latter subtle transition below pH 5.0 could be important for catalytic activity.

In the next step, we have addressed the nature of different pH-induced heme species in AncDyPD-b1 employing RR spectroscopy, which is highly sensitive to spin, coordination and the redox state of the heme group. High-frequency RR spectra acquired at pH values between 10.0 and 5.0 show spin/coordination marker bands, v_i, which are indicative of a ferric low spin (LS) state: v_4 at 1373 cm^{-1}, v_3 at 1502 cm^{-1}, v_2 at 1582 cm^{-1}, and $v_{C=C}$ at 1619 cm^{-1} [38]. The same frequencies are observed in the presence of CN$^-$ ligand (Fig. 5). These RR band frequencies suggest the presence of a strong sixth ligand (six coordinated LS, 6cLS
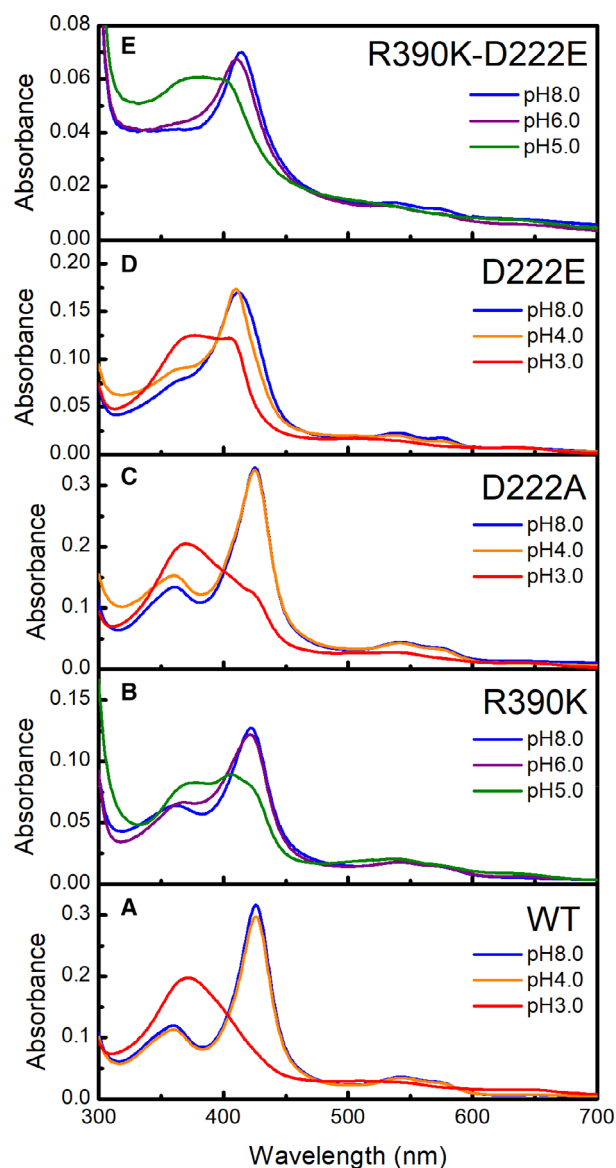

Fig. 4. UV-Vis spectra of AncDyPD-b1 (A) WT, (B) R390K, (C) D222A, (D) D222E, and (E) R390K-D222E at pH (blue) 8.0, (purple) 6.0, (green) 5.0, (orange) 4.0, and (red) 3.0. All spectra were recorded at 25 °C using 50 mM citric/phosphate buffers without other additives.

state) in the resting ferric AncDyPD-b1, most likely OH$^-$, H$_2$O, or some other small molecule (*vide infra*). This finding is consistent with the lack of catalytic activity of the enzyme at neutral pH, since the presence of the sixth axial ligand prevents H$_2$O$_2$ from binding to the active site, as already observed in some bacterial DyPs [39]. RR spectrum obtained at pH 3.5 reveals the presence of another species, indicated by downshifted components of v_3 and v_2 bands at 1488
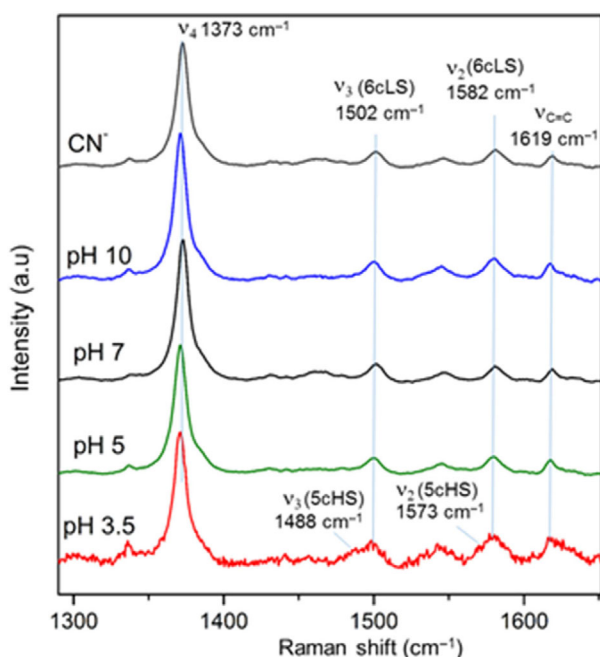
Fig. 5. Resonance Raman spectra of AncDyPD-b1 at pH 3.5, 5.0, 7.0, and 10.0 and in the presence of CN^- measured employing 413 nm excitation at 25 °C in the Britton–Robinson buffers.

and 1573 cm^{-1}, respectively, which can be attributed to a five coordinated high spin (5cHS) population. The catalytically competent 5cHS population [39,40] represents around 35 % in AncDyPD-b1 at pH 3.5, as judged by the comparison of the intensities of the two v_3 bands, which is consistent with the observed acidic optimum pH for enzyme activity. Interestingly, highly similar pH dependence of RR spectra has been recently reported for a C-type DyP from *Deinococcus radiodurans*, *Dr*DyP [39].

We can hence correlate the observed Soret band at 426 nm of AncDyPD-b1 with an inactive 6cLS species, while the active 5cHS population is most likely characterized by the observed 410 nm Soret band. Note that narrow bandwidths in RR spectra of AncDyPD-b1 at pH 5–10 indicate a presence of one uniform spin population. It is therefore not possible to address the nature of the species that gives origin to the 370 nm band (Fig. 4) by RR spectroscopy, most likely due to the insufficient (pre)resonance enhancement and/or low concentration. Moreover, the dramatic UV-Vis transition at low pH is slow (takes several minutes), while the activity measurements are obtained from initial rates (seconds). These results suggest that there is a rapid change in the heme microenvironment at low pH; most likely a release of a small molecule from the distal side of the heme. Consequently, the heme

switches from an inactive 6cLS state at neutral pH to an equilibrium with a highly active 5cHS population where the hydrogen peroxide molecule can bind to the distal side of the heme, triggering the catalytic mechanism. This rapid exchange at low pH is followed by a slow and reversible change that has a dramatic impact on the UV-Vis spectrum.

Steady-state kinetics

In order to study the peroxidase activity kinetics of AncDyPD-b1, we performed activity measurements at variable concentration of ABTS, RB5, RR2, DR80, DB71, RB19, and MnSO$_4$. The results revealed aberrant kinetic behavior for every substrate, including H$_2$O$_2$ (using ABTS as electron donor) (Fig. 6). The kinetic behaviors can be divided into four groups: (a) ABTS and anthraquinone dyes (DB71 and RB19) display substrate inhibition (S.I.); (b) azo dyes (RB5, RR2, and DR80) show strong cooperativity ($n \approx 3$), (c) there is also some cooperativity in the rate of H$_2$O$_2$ reduction ($n = 1.7$) and finally, (d) Mn^{2+} oxidation shows negative cooperativity ($n = 0.6$) (Table 1 and Data S2). The k_{cat} values vary widely from 0.04 to 22 s^{-1}, and the highest activity was found for ABTS, H$_2$O$_2$, and RB19 when compared to the other substrates. On the other hand, the K_M values are of the same magnitude, ranging between 3 and 40 μM, except for Mn^{2+}, which shows a relatively high K_M (80 mM).

Steady-state kinetic parameters obtained for AncAltDyPD-b1 using ABTS, RB5, DB71, RB19, and MnSO$_4$ were very similar to those observed for AncDyPD-b1, with substrate inhibition in the case of ABTS, DB71, and RB19, and different types of cooperativity for other substrates (Fig. S5 and Table S3). This demonstrates that the reconstruction is robust to uncertainties and that amino acids varying between AncDyPD-b1 and AncAltDyPD-b1 are not involved in the catalytic mechanism or in substrates recognition.

The k_{cat} values of AncDyPD-b1 are similar, while K_M values are higher compared with those of its only characterized descendent, *Ftr*DyP, which has also been tested using RB19, RB5, and ABTS [34]. Note that there was no report of nonideal kinetics for *Ftr*DyP. The catalytic efficiency (k_{cat}/K_M) of AncDyPD-b1 is higher for RB19, RB5, and ABTS by a factor of 40, 20, and 5, respectively. However, other D-type DyPs that are not descendants from AncDyPD-b1 show even higher catalytic efficiencies. For example, *Irpex lacteus* F17 DyP shows a k_{cat} of 8356 s^{-1} and a K_M of 62 μM for ABTS, and a k_{cat} of 5345 s^{-1} and a K_M of 133 μM for RB19 [41]. Interestingly, the activity
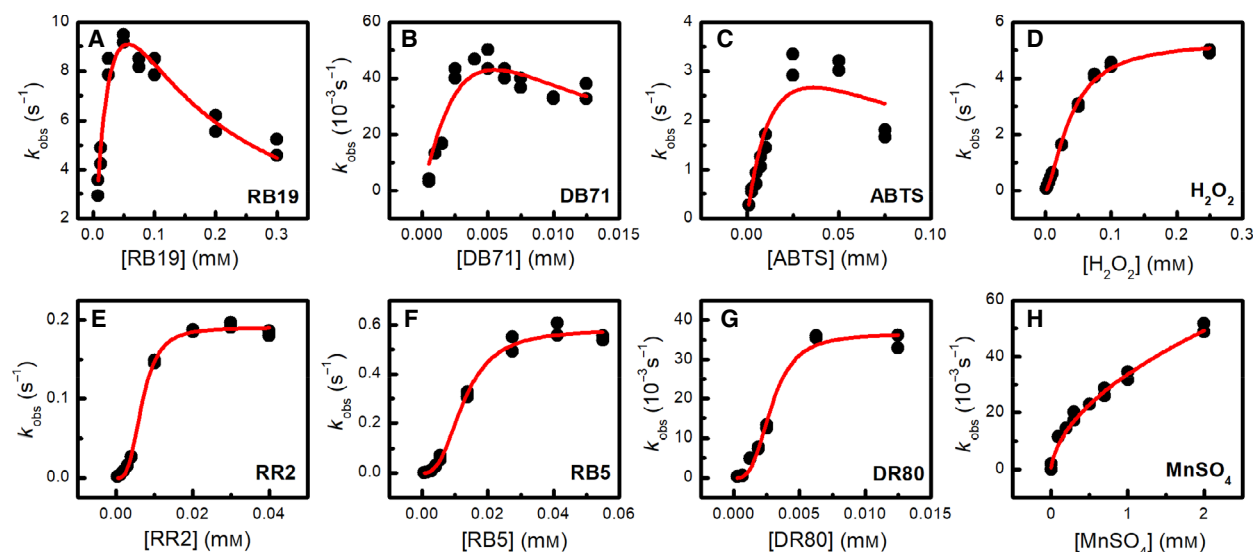
Fig. 6. AncDyPD-b1 k_{obs} *vs* substrate concentration for (A) RB19, (B) DB71, (C) ABTS, (D) H_2O_2, (E) RR2, (F) RB5, (G) DR80, and (H) MnSO$_4$. In red, fitted curves are shown employing either (A–C) substrate inhibition or (D–H) a cooperativity steady-state kinetics model described in equations (S2) and (S3) from Data S2. Experiments were performed at 25 °C using 50 mM citric/phosphate buffers without other additives.

Table 1. Steady-state kinetic parameters of WT AncDyPD-b1.

Substrate	Kinetic model	k_{cat} (s^{-1})	K_M (µM)	K_i (µM)	n	k_{cat}/K_M (s^{-1}·µM^{-1})
RB19	S.I.	22	42	78	–	0.53
DB71	S.I.	0.20	13	3	–	0.015
ABTS	S.I.	5.4	18	72	–	0.29
H_2O_2	Coop	5.4	39	–	1.6	0.14
RR2	Coop	0.19	6.8	–	3.2	0.028
RB5	Coop	0.58	13	–	2.7	0.046
DR80	Coop	0.04	2.9	–	3.2	0.013
Mn^{2+}	Coop	0.50	8×10^4	–	0.6	6.3×10^{-6}

of *Ftr*DyP was also tested for Mn^{2+} substrate, showing an efficiency that is far lower than the values observed from manganese peroxidases, but which is 500 times higher than AncDyPD-b1. Mn^{2+}-dependent degradation of lignin compounds has been reported and/or suggested for some DyPs [42,43]. As an ancestral enzyme, AncDyPD-b1 may be showing a common feature of the group, in line with the proposed physiological involvement of DyPs in lignin degradation.

Nonideal Michaelis–Menten kinetics, and particularly cooperativity, are usually associated with multimeric enzymes. However, gel permeation chromatography of AncDyPD-b1 and its elucidated crystal structure (*vide infra*) revealed that it is a monomeric enzyme. Thus, the observed aberrant kinetics could be a result of a multiple ligand-binding site

enzyme and/or an interplay between scaffold dynamics and catalytic mechanisms [44,45]. Nevertheless, mechanisms such as the mnemonic model have explained comparable results in single ligand-binding site enzymes, so the latter case cannot be discarded [45]. It is noteworthy that DyPs have shown capability to oxidize bulky substrates that are not able to enter into the heme pockets [5]. It has been proposed that one or more exposed aromatic residues may act as catalytic sites, leading to a low substrate specificity [33,46]. Such sites are usually distant from the heme cofactor, involving long intraprotein electron transfer pathways. Consistent with a presence of one or more exposed sites, AncDyPD-b1 displays high substrate promiscuity. Moreover, the kinetic parameters obtained from similar dyes show no correlation with the substrate size (Table 1).

The steady-state kinetic parameters for H_2O_2, ABTS and RB5 were also obtained for the five AncDyPD-b1 mutants (Table 2). Nonideal kinetics were also observed for all of them (Fig. S6), and the optimum pH for activity was found to be the same (Fig. S4). An overview of the steady-state parameters is summarized in Table 2. It is observed that the nonconservative variants display much lower peroxidase activity, while conservative mutations have little effect. Considering that the mutations assessed in this work alter the heme microenvironment, we anticipated to see a significant impact on the reduction in hydrogen peroxide.

Table 2. Steady-state kinetic parameters of AncDyPD-b1 variants for ABTS, RB5, and H_2O_2[a].

AncDyPD-b1	ABTS				RB5				H_2O_2[a]			
	k_{cat} (s^{-1})	K_M (μM)	K_i (μM)	k_{cat}/K_M (s$^{-1}\cdot\mu$M^{-1})	k_{cat} (s^{-1})	K_M (μM)	N	k_{cat}/K_M (s$^{-1}\cdot\mu$M^{-1})	k_{cat} (s^{-1})	K_M (μM)	n	k_{cat}/K_M (s$^{-1}\cdot\mu$M^{-1})
WT	5.4	18	72	0.29	0.58	13	2.7	0.046	5.4	39	1.6	0.14
R390A	0.14	11	190	0.012	0.11	6	1	0.018	0.47	4180	1	1.1×10^{-4}
D222A	0.036	0.23	79	0.15	0.002	4.2	2.8	4.5×10^{-4}	0.28	1930	1	1.4×10^{-4}
R390K	7.1	13	47	0.53	0.12	13	2.1	0.0089	13.6	31	1.2	0.44
D222E	2.5	3.3	90	0.77	0.038	8.9	2.2	0.0042	4.3	95	1.4	0.045
R390K-D222E	5	15	32	0.33	0.015	10	2.3	0.0015	1.6	61	2.2	0.026

[a]H_2O_2 activity was assessed employing ABTS as electron donor.

Consequently, the catalytic efficiencies for H_2O_2 reduction in the nonconservative variants were lowered by about 3 orders of magnitude, while the conservative variants were mildly affected. In fact, the R390K AncDyPD-b1 mutant was slightly more active toward hydrogen peroxide, while both D222E containing AncDyPD-b1 mutants displayed lower efficiencies when compared to the WT enzyme. This may suggest a mechanistic role of the distal aspartate in the H_2O_2 reduction mechanism.

Interestingly, ABTS oxidation efficiency is only significantly affected by the nonconservative R390A mutation. Nonetheless, the D222A mutant displayed a 150-fold lower k_{cat}, while the K_M decreased 80-fold. In the case of RB5 oxidation, the catalytic efficiency is lower for every variant, but the aspartate variants show more severe impact than the arginine variants. Given the size of the tested substrates, the oxidation event necessarily occurs at a distant site to the heme [10,33]. The entire catalytic process could be simplified into a three-step scheme: oxidation of the organic compound at the exposed oxidation site, intraprotein electron transfer, and H_2O_2 reduction at the heme. It is very unlikely that mutations at the heme can directly affect the oxidation step at a distant site. However, H_2O_2 reduction k_{cat} values are comparable to those of ABTS oxidation, but one or more orders of magnitude higher than k_{cat} values for RB5 oxidation. These results suggest that H_2O_2 reduction could be the rate-limiting step in ABTS oxidation, but in the case of RB5 oxidation, the limiting step may be the intraprotein electron transfer. Hence, it appears that the distal aspartate participates in the intraprotein electron transfer. Previous studies on *Aau*DyPI suggested that the distal aspartate is not involved in the electron transfer pathway but acts as a conformational switch that facilitates the electron transfer from the oxidation site to the heme [33,47]. Our findings are in good agreement with this hypothesis, leading us to propose that such mechanism could be a common feature of D-type DyPs.

Last but not least, the mutants in which the arginine was replaced showed lower stability, which may reflect increased scaffold flexibility. Recent works have shown that the more flexible the scaffold, the higher the activation barrier of long-range electron transfer processes tends to be in proteins [48,49]. Such effect was described for several metalloenzymes, including heme-containing cytochrome *c* [50,51]. Thus, although a direct mechanistic role cannot be excluded, the distal arginine may be important for tuning the structural dynamics for the internal electron transfer process.

Structural Characterization

The crystal structure of reconstructed ΔAncDyPD-b1 (residues 24–511) was determined at 1.7 Å resolution and has the typical D-type DyP family topology (Fig. 7). The residues 85–97, 145–149, and 258–260 situated in surface loops, are not visible in electron density. The enzyme is monomeric as most other members of the D-type DyP family. ΔAncDyPD-b1 shows 65% identity to *Pos*DyP4 [52] (PDB: 6FSK, RMSD 1.0 Å), 56% to *Bad*DyP [12] (PDB: 2D3Q, RMSD 1.0 Å), and 51% to *Aau*DyPI (PDB: 4W7J, RMSD 1.2 Å) [33]. The ancestor is also 34 % identical to DyP2 from *Amycolatopsis* [42] (*Amy*Dyp2, PDB: 4G2C, RMSD 1.8 Å) and to *Anabaena* DyP-type peroxidase (*Ana*PX, PDB: 5C2I, RMSD 1.9 Å, tetramer) [53]. ΔAncDyPD-b1 and *Pos*DyP4 have longer loops and are ~ 50 residues larger than the latter four enzymes. Note that the first 23 residues of AncDyPD-b1 are deleted in ΔAnc-DyPD-b1 and the Pro24 is mutated to an alanine (see Materials and methods). Ala24 is located at a similar location as the N termini of *Aau*DypI, *Bad*DyP and *Pos*DyP4, suggesting that the first 23 N-terminal residues in AncDyPD-b1 are not part of the core structure. In fact, this N-terminal region may normally
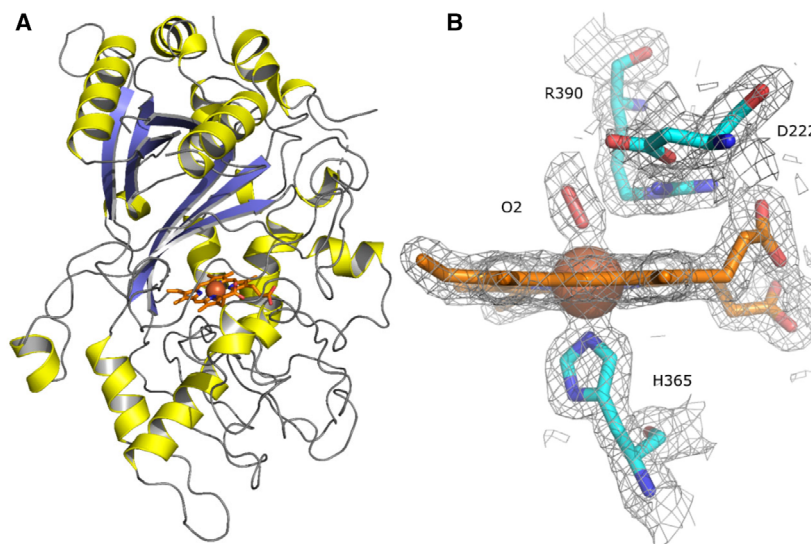
Fig. 7. (Left) The overall fold of the ΔAncDyPD-b1 structure showing the heme (orange) and iron (brown) at the active site. The α-helices are shown in yellow and the β-sheets in slate blue. (Right) The σ-weighted 2mFo-DFc electron density using phases from the final model is contoured at 1.0 σ level. Contours more than 2.2 Å from any of the displayed atoms have been removed for clarity. A dioxygen molecule (red) is modeled near the heme cofactor. The figure was prepared by using PYMOL (Schrödinger).

harbor the secretion signal for extracellular expression. However, when the first 100 amino acids in the protein sequence were analyzed by using the TatP 1.0 Server [54], no Tat-signal sequence was detected (Fig. S7). The truncated variant, ΔAncDyPD-b1, crystallized much faster and resulted in crystals with superior diffraction properties. It is possible that these 23 amino acids once played a role in type C DyPs and through evolution and horizontal gene transfer became an integral part of type D DyPs. However, for establishing the reason for the formation of low-quality crystals in the presence of the first 23 amino acids further investigation would be required.

Despite the Mn^{2+} peroxidase activity measured for AncDyPD-b1, the ΔAncDyPD-b1 structure is lacking the Mn^{2+}-binding site observed in *Amy*DyP2 [42]. Also, the presumed Mn^{2+}-binding site in *Pos*DyP4, containing three aspartates and one glutamate [52], is absent in ΔAncDyP-b1. This explains the relatively low activity of the ancestral DyP and may hint to a relative recent event in this clade by which extant D-type DyPs have acquired Mn^{2+} oxidation activity.

The X-ray structure reveals that the heme cofactor is ligated by conserved residues: on the proximal side by His365-Nε, while Asp222, Arg390, Leu415, and Phe417 line up the distal side (Fig. 7B). Interestingly, at the distal face a diatomic ligand is bound, almost vertically to the heme plane. It has been previously suggested as a dioxygen molecule arising from photoreduction of the iron by X-ray exposure [55]. A very similar complex with dioxygen has been reported for horseradish peroxidase (PDB: 1H57) where it was shown that X-rays induce formation of such a complex. However, note that the enzyme is redox and

catalytically inactive at neutral pH (*vide supra*) and that RR data also indicate that a strong ligand is bound to the ferric heme at pH > 3.5, which is responsible for 6cLS state of the heme and AncDyP-b1 catalytic inactivity. Although it is not clear at this point whether the same ligand occupies the 6th axial position of the heme in solution and crystal state, it is tempting to speculate that the enzyme is actually trapped in compound III state (ferric-peroxo complex, $[Fe^{3+}- O_2]^-$) and becomes catalytically active only upon detachment of the 6th axial ligand triggered by a change in local pH or some other physiological stimulus. The Nη2 of Arg390 is hydrogen bonded to the backbone carbonyl of Ser225 and to a propionyl group of the heme, while the Nη1 has hydrogen bonds to Oδ1 of Asp222 and to the proximal atom of the dioxygen. The distance of the carboxylate atoms of Asp222 to the dioxygen is long (4.1/4.6 Å) indicating a minor interaction. The oxygen-binding site is the site where H_2O_2 would bind to the heme. The elucidated dioxygen-complexed structure provides a good model for understanding the geometry by which a ligand can bind.

Conclusions

In the present article, several D-type DyP ancestors have been reconstructed employing ASR. Among them, AncDyPD-b1 has been overexpressed in *E. coli* and purified in high yields as a heme-containing, soluble, and active peroxidase. By addressing the ambiguously reconstructed sites, we obtained a variant with 88 different residues, mostly placed on the protein surface. Both enzymes are stable at room temperature

and present almost identical spectroscopic, structural, and functional features, showing the robustness and reliability of the ASR procedure. The UV-Vis spectrum of AncDyPD-b1 reveals the general features of a heme protein although its Soret band (426 nm) is red-shifted when compared with typical hemoproteins. There are no spectral changes upon addition of oxidants, reductants, or potential ligands, suggesting that the atypical Soret band position may reflect other details of the heme electronic structure. Interestingly, there is a slow transition at acid pH with a dramatic but fully reversible effect on the UV-Vis spectrum.

AncDyPD-b1 is capable of oxidizing a wide variety of substrates with moderate efficiency compared with other D-type DyPs, while it is not able to perform sulfoxidations. RR experiments indicate that the low optimum pH for peroxidase activity is associated with a significant population of a high spin state (5cHS) species. The elucidated crystal structure is consistent with the spectroscopic data and reveals characteristic features of D-type DyPs confirmed by a good degree of similarity with previous reports. Interestingly, AncDyPD-b1 lacks a Mn^{2+}-binding site, even though Mn^{+2} peroxidase activity was found, suggesting a recently acquired Mn^{2+} oxidation capability. This is a feature shared by other DyPs, which has been linked to a role in lignin degradation.

Five site-directed AncDyPD-b1 mutants were generated to explore the role of the aspartate (D222) and arginine (R390) heme distal residues. UV-Vis spectra revealed similar features to those of the WT enzyme, but variable Soret band positions. This highlights the role of both residues in fine-tuning the cofactor electronic structure. Nonconservative mutations (D222A and R390A) show a dramatic impact in the efficiency of H_2O_2 reduction. On the other hand, replacement of R390 resulted in lower heme incorporation, lower stability, and a higher pH for the UV-Vis transition, while replacing D222 had a stronger lowering effect on peroxidase activity. Our results demonstrate that both ligands are essential for the H_2O_2 reduction mechanism at the heme site. They also suggest that the distal aspartate plays a key role in the intraprotein long-range electron transfer, as was already proposed for another D-type DyP, *Auricularia auricula–judae* DyP. The arginine also seems to affect the intraprotein electron transfer, but in a more nonspecific way; through modulation of the scaffold dynamics, a general phenomenon recently described in cupredoxins and already observed in other heme-containing enzymes, e.g., cytochrome *c*.

This work, to the best of our knowledge, represents the first study of the role of distal aspartate and arginine residues in a D-type DyP. Finally yet importantly, the ease of expression and stability of AncDyPD-b1 for biochemical experiments offers an opportunity to deepen our knowledge about fungal DyPs and to advance our understanding on DyP-type-dependent characteristics of this still largely unexplored superfamily of peroxidases.

Materials and methods

Phylogenetic analysis and ancestral sequence reconstruction

A dataset of DyP sequences was initially formed by the InterPro family IPR006314 named DyP-type peroxidase ($\approx$ 14 000 sequences, last accession August 2018) plus the dataset gathered by Colpa *et al.* [56]. In order to get a representative and nonredundant group of sequences, the following steps were performed successively: (a) removing redundancy by CD-HIT (initial sequence identity cut-off 90%), (b) multiple sequence alignment in MAFFT v7, (c) inferring relationships by neighbor-joining method, and (d) manual inspection. All these steps were carried out employing the MAFFT suite [57]. The final dataset included 641 sequences. The best-fit model parameters were obtained by the Akaike information criterion in PROTTEST v3.4.[58] Phylogeny was inferred by maximum likelihood method in PHYML v3.0. 500 [59]. Bootstraps were run followed by bootstrap transfer in BOOSTER [60].

Ancestral sequence reconstruction was performed in PAMLX v.4.9 [61]. Analysis was done using an empirical amino acid substitution model (model = 2), four gamma categories, and the Jones substitution matrix. The posterior probability (PP) distribution of ancestral states at each site was analyzed at targeted nodes. Sites were considered ambiguously reconstructed if alternative states displayed PP > 0.2. The sequence length of ancestors was determined by parsimony.

Enzyme expression and purification

The genes for expression of AncDyPD-b1, AncAltDyPD-b1, and AncDyPD-b2 were ordered as codon-optimized genes for expression in *E. coli* with *BsaI* overhangs (Thermo Fisher Scientific, Waltham, MA, USA). The sequences are provided in the supporting information (Data S3). Each gene was cloned using the golden gate assembly method into a pBAD vector resulting in expression of the target protein with a His-tag at the N terminus followed by a SUMO fusion protein. Given that AncDyPD-b1 crystals were not good for high-quality X-ray diffraction data (*vide infra*), a truncated version of AncDyPD-b1 was expressed (ΔAncDyPD-b1). The expression vector for this was prepared by deleting the coding region for the first 23 N-terminal residues and introducing a P24A mutation to allow

cleavage of the SUMO-tag by SUMO protease. The constructs' expression was carried out in *E. coli* NEB 10β competent cells (New England Biolabs) grown overnight at 37 °C on Luria–Bertani (LB) plates supplemented with 50 μg·mL^{-1} ampicillin. A single colony was picked from the plate and used to inoculate a 5 mL preculture of LB medium supplemented with ampicillin at a final concentration of 50 μg·mL^{-1}. The preculture was then used to inoculate 500 mL terrific broth medium (TB) in a 2-L Erlenmeyer flask. The 500 mL culture was supplemented with ampicillin to reach a final concentration of 50 μg·mL^{-1} and grown at 37 °C until the OD reached a value of 0.6 (approximately 3 h). Arabinose was added for induction to attain a final concentration of 0.02% w/v. The culture was then grown at 25 °C for 18 h. After that, the cells were harvested by centrifuging the culture at 6000 *g* at 4 °C for 20 min. The cells were then resuspended in 15 mL of buffer A (50 mM potassium phosphate buffer, 0.5 M NaCl, 5% [v/v] glycerol, pH 8) and lysed by sonication for 10 min with cycles of 10 s ON and 10 s OFF at 70% amplitude. The lysate was centrifuged at 18 500 *g* for 30 min at 4 °C and the cell-free extract filtered through a Whatman FP 30/0.45 μm CA-S membrane syringe filter.

The cell-free extract was loaded using an AKTA Pure system (Chicago, IL, USA) onto a 5-mL Ni-Sepharose prepacked column, which had been equilibrated using 5 column volumes of buffer A. After that, the column was washed with 5 column volumes of buffer A followed by 5 column volumes of buffer B (50 mM potassium phosphate buffer, 0.5 M NaCl, 5% [v/v] glycerol, 10 mM imidazole, pH 8). The protein was finally eluted using buffer C (50 mM potassium phosphate buffer, 0.5 M NaCl, 5% v/v glycerol, 500 mM imidazole, pH 8) until all the protein was washed off the column (usually 5 mL). The protein was desalted using an Econo-Pac® 10DG desalting prepacked gravity flow column (Bio-Rad, Hercules, CA, USA) using buffer D (50 mM potassium phosphate buffer, 150 mM NaCl, 10% v/v glycerol, pH 7.5). The desalted protein fractions were analyzed by SDS/PAGE followed by staining using InstantBlue™ Protein Stain, to assess purity and size of the purified protein.

For SUMO cleavage of AncDyPD-b1 and its mutants, SUMO protease was used. It was added to the desalted sample solution to a final ratio protease/enzyme (mg·mg^{-1}) of 1/200 and left on a 3D gyratory mixer at 4 °C overnight. Then, it was loaded onto a Ni-sepharose column as described before using an AKTA Pure System and the red-colored flow-through was desalted as described before (*vide supra*). The cleaved SUMO protein and SUMO protease were both trapped in the resin due to their His tags. For lyophilization of AncDyPD-b1, the sample buffer was changed to 50 mM Tris/HCl pH 7.5, 150 mM NaCl, 20 mg·mL^{-1} sucrose, and 25 mM MgSO$_4$.

Site-directed mutagenesis

Site-directed mutagenesis was performed for D222 and R390 by the QuikChange method. PCR mix (30 μL final)

contained 15 μL PfuUltra II Hotstart PCR Master Mix, 2 μL primer mix (10 μM), 1 μL plasmid (5 μM), and 12 μL milli-Q water. After a standard PCR program was completed, 1 μL of *Dpn*I solution was added for 2 h incubation at 37 °C and then 20 min at 80 °C (to inactivate *Dpn*I). All the mutagenesis primers used in this work are detailed in Data S1. For the double variant AncDyPD-b1 R390K/D222E, the plasmid containing the gene for expression of variant AncDyPD-b1 D222E was used as a template and the protocol for generating the R390K mutation was followed. For obtaining ΔAncDyPD-b1, we first obtained a AncDyPD-b1 variant without the first 23 amino acids, and then, the plasmid containing the gene for its expression was used as a template for generating the P24A mutation. The sequence of each mutated gene was confirmed by DNA sequencing and the mutant gene expressed as described above for wild-type (WT) AncDyPD-b1.

UV-Vis spectral analysis

All purified enzymes were analyzed by UV-Vis absorption spectroscopy (V-660 spectrophotometer, Jasco, Easton, MD, USA). Absorbance spectra were recorded between 200 and 700 nm at 25 °C. Enzyme concentrations were determined using a predicted molecular extinction coefficient at 280 nm in ProtParam tool [62], $\varepsilon_{280} = 29.575$ mM^{-1}·cm^{-1} for AncDyPD-b1, and it was used for all mutants.

Resonance Raman spectroscopy

Resonance Raman (RR) spectra were acquired using a confocal Raman spectrometer (Jobin-Yvon LabRam 800 HR, HORIBA, Minamu-ku Kyoto, Japan) equipped with a liquid nitrogen-cooled CCD detector, employing 413 nm excitation from a krypton ion laser (Coherent INNOVA 300c; Coherent, Palo Alto, CA, USA). Spectra were measured from 100 μL of 100 μM protein placed into a rotating cuvette (Hellma, Mullheim, Germany) to prevent prolonged exposure of individual enzyme molecules to laser irradiation. Spectra were recorded with 2.5 mW laser power and 15- to 25-s accumulation times and spectral resolution of 0.7 cm^{-1}; typically 4–10 spectra were co-added in each measurement to improve signal-to-noise ratio. pH-dependent RR spectra were obtained using phosphate (pH 7.0) or Britton–Robinson buffers (pH 3.5; 5.0; 7.5; and 10.0); an excess of pH adjusted KCN (pH 8.0) solution was used to generate CN$^-$ bound heme species.

Steady-state kinetics

The enzymatic activity of AncDyPD-b1 and its variants was monitored using a Jasco V-660 spectrophotometer. Assays were performed at least in duplicates, at 25 °C in 50 mM sodium citrate buffer at optimal pH (3.0 for 2,2'-azino-bis(3-ethylbenzothiazoline-6-sulfonic acid) [ABTS] and 4.0 for other substrates) and using hydrogen peroxide

at a final concentration of 100 μM unless otherwise stated. For starting the reaction, enzyme was added to a final concentration between 50 and 500 nM. When activity was low, the enzyme concentration was raised up to 2.0 μM. Activity values were corrected by protein relative heme content for steady-state analysis of every variant.

Substrates were tested at varying concentrations to determine the steady-state parameters (K_M, k_{cat} and K_i or n, depending on the case) for each one. Assessed substrates were ABTS, Reactive Black 5 (RB5), Reactive Red 2 (RR2), Direct Red 80 (DR80), Direct Blue 71 (DB71), Reactive Blue 19 (RB19), and MnSO$_4$. Steady-state kinetics of hydrogen peroxide reduction was determined using ABTS at a concentration of maximum activity (below substrate inhibition) which is 10 μM for D222A, D222E, and R390K-D222E, 25 μM for R390K and WT, and 50 μM for R390A. The reported maximum absorbance wavelength and its extinction coefficient for used dyes were corroborated by UV-Vis measurements and standard calibration curves, respectively. Mn^{2+} peroxidation was followed by monitoring Mn^{3+} malonate formation at 270 nm (ε_{270} = 11.6 mM^{-1}·cm^{-1}). The assay was performed using a series of dilutions of MnSO$_4$ in 0.1 M sodium malonate buffer of pH 4.5 at 25 °C, and the reaction was started by the addition of 100 μM hydrogen peroxide. In all the activity assays, controls were performed without the addition of enzyme and no significant activity was detected in any case. ORIGINPRO 8.1 software (OriginLab Corporation, Northampton, MA, USA) was used for the analysis, and models are described in Data S2.

Crystallization, Data Collection, Structure Determination, and Refinement

AncDyPD-b1 WT was further purified by gel filtration chromatography at 7 °C using a Superdex 75 10/300 GL column (Cytiva, Marlborough, MA, USA), equilibrated with 20 mM HEPES buffer, pH 7.3, containing 150 mM NaCl. The fractions containing the enzyme, eluting at 50 kDa, were pooled and concentrated. Initial sitting-drop crystallization screening was performed using a Mosquito crystallization robot (TTP LabTech) in a 96-well MRC2 plate (SWISSCI) with a protein concentration of ~ 16 mg·mL^{-1}. Many commercially available screening solutions were tested for crystallization experiments. Crystals appeared after 6 months of incubation at 294 K in solutions B1-B3 from the LMB screen (molecular dimensions) containing 1.6–1.95 M ammonium sulfate and 0.1 M MES or 0.1 M citrate buffer pH 6.5. The crystals were fragile and had tendency to stick to the plate. Prior to data collection, a crystal was briefly soaked in a cryoprotectant solution containing 2.2 M ammonium sulfate, 0.1 M MES buffer pH 6.5, and 30% glycerol and flash-cooled in liquid nitrogen. X-ray diffraction data were collected at beamline i04 at the Diamond Light Source and processed using XDS. The AncDyPD-b1 crystal belonged to an orthorhombic space group with a = 53.0 Å, b = 69.5 Å, and c = 117.0 Å and diffracted to 2.9 Å. The space group and preliminary structure of AncDyPD-b1 WT were determined by the molecular replacement method (MR) using PHASER [63] with mixed model coordinates of *Pleurotus ostreatus* heme-containing DyP-type peroxidase [52] (PDB: 6FSK) as search model. Phaser found a solution for space group P2$_1$2$_1$2$_1$ with one monomer in the asymmetric unit. The model was refined with Refmac5 [64,65] and Phenix, and Coot [66] was used for manual rebuilding and map inspection. The X-ray data of the AncDyPD-b1 WT showed no electron density for the first 23 amino acids. A truncated mutant, ΔAncDyPD-b1, in which the 23 N-terminal residues were deleted and a P24A mutation was produced and purified. ΔAncDyPD-b1 crystallized readily in ammonium sulfate at pH 6.5, and conditions were optimized to obtain single crystals. X-ray diffraction data were collected at beamline i03 at the Diamond Light Source and autoprocessed with Dials [67]. The ΔAncDyPD-b1 crystal also belonged to space group no. 19 with a = 59.1 Å, b = 69.1 Å, and c = 114.4 Å and diffracted to 1.7 Å. The V_M is 2.1 Å^3/Da [68] with a solvent content of 42 %. Data collection statistics are listed in Table S1. MR was performed with the low-resolution AncDyPD-b1 structure as a search model, and the structure was refined with Refmac5 and Phenix. Three TLS (translation/libration/screw) groups per monomer were used in the last rounds of refinement. The quality of the model was analyzed with PDB-REDO [69] and MolProbity [70]. Atomic coordinates and experimental structure factor amplitudes have been deposited in the Protein Data Bank (PDB: 7ANV) (see Table S1).

Conflict of interest

The authors declare no conflict of interest.

Author contributions

UAZ conceptualized the data, investigated enzyme production, variants design, UV-Vis, steady-state kinetics, and wrote the original draft. MHH investigated enzyme production, UV-Vis, and steady-state kinetics. HR investigated crystal structure. MLM investigated ancestral sequence reconstruction. ST investigated resonance Raman. MWF conceptualized the data, supervised the project, and acquired funding.

Peer Review

The peer review history for this article is available at https://publons.com/publon/10.1111/febs.15687.

References

1 Sugano Y (2009) DyP-type peroxidases comprise a novel heme peroxidase family. *Cell Mol Life Sci* **66**, 1387–1403.

2 Kim SJ & Shoda M (1999) Purification and characterization of a novel peroxidase from *Geotrichum candidum* Dec 1 involved in decolorization of dyes. *Appl Environ Microbiol* **65**, 1029.

3 Falade AO & Ekundayo TC (2020) Emerging biotechnological potentials of DyP-type peroxidases in remediation of lignin wastes and phenolic pollutants: a global assessment (2007–2019). *Lett Appl Microbiol*. https://doi.org/10.1111/lam.13392

4 Lončar N, Colpa DI & Fraaije MW (2016) Exploring the biocatalytic potential of a DyP-type peroxidase by profiling the substrate acceptance of *Thermobifida fusca* DyP peroxidase. *Tetrahedron* **72**, 7276–7281.

5 Roberts JN, Singh R, Grigg JC, Murphy MEP, Bugg TDH & Eltis LD (2011) Characterization of dye-decolorizing peroxidases from *Rhodococcus jostii* RHA1. *Biochemistry* **50**, 5108–5119.

6 Krahe N-K, Berger RG & Ersoy F (2020) A DyP-type peroxidase of *Pleurotus sapidus* with alkene cleaving activity. *Molecules* **25**, 1536.

7 Fawal N, Li Q, Savelli B, Brette M, Passaia G, Fabre M, Mathé C & Dunand C (2012) PeroxiBase: a database for large-scale evolutionary analysis of peroxidases. *Nucleic Acids Res* **41**, D441–D444.

8 Yoshida T & Sugano Y (2015) A structural and functional perspective of DyP-type peroxidase family. *Arch Biochem Biophys* **574**, 49–55.

9 Sutter M, Boehringer D, Gutmann S, Günther S, Prangishvili D, Loessner MJ, Stetter KO, Weber-Ban E & Ban N (2008) Structural basis of enzyme encapsulation into a bacterial nanocompartment. *Nat Struct Mol Biol* **15**, 939–947.

10 Colpa DI, Fraaije MW & van Bloois E (2014) DyP-type peroxidases: a promising and versatile class of enzymes. *J Ind Microbiol Biotechnol* **41**, 1–7.

11 Gajhede M, Schuller DJ, Henriksen A, Smith AT & Poulos TL (1997) Crystal structure of horseradish peroxidase C at 2.15 Å resolution. *Nat Struct Mol Biol* **4**, 1032–1038.

12 Zámocký M, Hofbauer S, Schaffner I, Gasselhuber B, Nicolussi A, Soudi M, Pirker KF, Furtmüller PG & Obinger C (2015) Independent evolution of four heme peroxidase superfamilies. *Arch Biochem Biophys* **574**, 108–119.

13 Goblirsch B, Kurker RC, Streit BR, Wilmot CM & DuBois JL (2011) Chlorite dismutases, DyPs, and EfeB: 3 microbial heme enzyme families comprise the CDE structural superfamily. *J Mol Biol* **408**, 379–398.

14 Sugano Y, Muramatsu R, Ichiyanagi A, Sato T & Shoda M (2007) DyP, a unique dye-decolorizing peroxidase, represents a novel heme peroxidase family: ASP^{171} replaces the distal histidine of classical peroxidases. *J Biol Chem* **282**, 36652–36658.

15 Habib MH, Rozeboom HJ & Fraaije MW (2019) Characterization of a new DyP-peroxidase from the alkaliphilic cellulomonad, Cellulomonas bogoriensis. *Molecules* **24**, 1208.

16 Yoshida T, Tsuge H, Konno H, Hisabori T & Sugano Y (2011) The catalytic mechanism of dye-decolorizing peroxidase DyP may require the swinging movement of an aspartic acid residue: catalytic residue Asp171 swings in view. *FEBS J* **278**, 2387–2394.

17 Liu X, Du Q, Wang Z, Zhu D, Huang Y, Li N, Wei T, Xu S & Gu L (2011) Crystal structure and biochemical features of EfeB/YcdB from *Escherichia coli* O157: ASP^{235} plays divergent roles in different enzyme-catalyzed processes. *J Biol Chem* **286**, 14922–14931.

18 Singh R, Grigg JC, Armstrong Z, Murphy MEP & Eltis LD (2012) Distal heme pocket residues of B-type dye-decolorizing peroxidase: arginine but not aspartate is essential for peroxidase activity. *J Biol Chem* **287**, 10623–10630.

19 Rahmanpour R, Rea D, Jamshidi S, Fülöp V & Bugg TDH (2016) Structure of *Thermobifida fusca* DyP-type peroxidase and activity towards Kraft lignin and lignin model compounds. *Arch Biochem Biophys* **594**, 54–60.

20 Chen C, Shrestha R, Jia K, Gao PF, Geisbrecht BV, Bossmann SH, Shi J & Li P (2015) Characterization of dye-decolorizing peroxidase (DyP) from *Thermomonospora curvata* reveals unique catalytic properties of A-type DyPs. *J Biol Chem* **290**, 23447–23463.

21 Mendes S, Catarino T, Silveira C, Todorovic S & Martins LO (2015) The catalytic mechanism of A-type dye-decolourising peroxidase BsDyP: neither aspartate nor arginine is individually essential for peroxidase activity. *Catal Sci Technol* **5**, 5196–5207.

22 Uchida T, Sasaki M, Tanaka Y & Ishimori K (2015) A dye-decolorizing peroxidase from *Vibrio cholerae*. *Biochemistry* **54**, 6610–6621.

23 Mendes S, Brissos V, Gabriel A, Catarino T, Turner DL, Todorovic S & Martins LO (2015) An integrated view of redox and catalytic properties of B-type PpDyP from Pseudomonas putida MET94 and its distal variants. *Arch Biochem Biophys* **574**, 99–107.

24 Alessa AHA, Tee KL, Gonzalez-Perez D, Omar Ali HEM, Evans CA, Trevaskis A, Xu J-H & Wong TS (2019) Accelerated directed evolution of dye-decolorizing peroxidase using a bacterial extracellular protein secretion system (BENNY). *Bioresour Bioprocess* **6**, 20.

25 Krainer FW, Gerstmann MA, Darnhofer B, Birner-Gruenberger R & Glieder A (2016) Biotechnological advances towards an enhanced peroxidase production in Pichia pastoris. *J Biotechnol* **233**, 181–189.

26 Behrens CJ, Zelena K & Berger RG (2016) Comparative cold shock expression and characterization of fungal dye-decolorizing peroxidases. *Appl Biochem Biotechnol* **179**, 1404–1417.

27 Zuckerkandl E & Pauling L (1965) Molecules as documents of evolutionary history. *J Theor Biol* **8**, 357–366.

28 Liberles DA (ed.) (2007) Ancestral Sequence Reconstruction. Oxford University Press, Oxford; New York.

29 Hochberg GKA & Thornton JW (2017) Reconstructing ancient proteins to understand the causes of structure and function. *Annu Rev Biophys* **46**, 247–269.

30 Ayuso-Fernández I, Martínez AT & Ruiz-Dueñas FJ (2017) Experimental recreation of the evolution of lignin-degrading enzymes from the Jurassic to date. *Biotechnol Biofuels* **10**, 67.

31 Ayuso-Fernández I, De Lacey AL, Cañada FJ, Ruiz-Dueñas FJ & Martínez AT (2019) Increase of redox potential during the evolution of enzymes degrading recalcitrant lignin. *Chem Eur J* **25**, 2708–2712.

32 Ayuso-Fernández I, Ruiz-Dueñas FJ & Martínez AT (2018) Evolutionary convergence in lignin-degrading enzymes. *Proc Natl Acad Sci USA* **115**, 6428–6433.

33 Strittmatter E, Liers C, Ullrich R, Wachter S, Hofrichter M, Plattner DA & Piontek K (2013) First crystal structure of a fungal high-redox potential dye-decolorizing peroxidase: substrate interaction sites and long-range electron transfer. *J Biol Chem* **288**, 4095–4102.

34 Kolwek J, Behrens C, Linke D, Krings U & Berger RG (2018) Cell-free one-pot conversion of (+)-valencene to (+)-nootkatone by a unique dye-decolorizing peroxidase combined with a laccase from *Funalia trogii*. *J Ind Microbiol Biotechnol* **45**, 89–101.

35 Kung C-P, Wu Y-R & Chuang H (2014) Expression of a dye-decolorizing peroxidase results in hypersensitive response to cadmium stress through reducing the ROS signal in Arabidopsis. *Environ Exp Bot* **101**, 47–55.

36 ten Have R & Teunissen PJM (2001) Oxidative mechanisms involved in lignin degradation by white-rot fungi. *Chem Rev* **101**, 3397–3414.

37 van Bloois E, Torres Pazmiño DE, Winter RT & Fraaije MW (2010) A robust and extracellular heme-containing peroxidase from *Thermobifida fusca* as prototype of a bacterial peroxidase superfamily. *Appl Microbiol Biotechnol* **86**, 1419–1430.

38 Todorovic S (2019) Raman biospectroscopy and imaging. In Radiation in Bioanalysis (Pereira AS, Tavares P & Limão-Vieira P, eds), pp. 111–145. Springer International Publishing, Cham.

39 Silveira CM, Moe E, Fraaije M, Martins LO & Todorovic S (2020) Resonance Raman view of the active site architecture in bacterial DyP-type peroxidases. *RSC Adv* **10**, 11095–11104.

40 Sezer M, Santos A, Kielb P, Pinto T, Martins LO & Todorovic S (2013) Distinct structural and redox properties of the heme active site in bacterial dye decolorizing peroxidase-type peroxidases from two subfamilies: resonance Raman and electrochemical study. *Biochemistry* **52**, 3074–3084.

41 Duan Z, Shen R, Liu B, Yao M & Jia R (2018) Comprehensive investigation of a dye-decolorizing peroxidase and a manganese peroxidase from Irpex lacteus F17, a lignin-degrading basidiomycete. *AMB Expr* **8**, 119.

42 Brown ME, Barros T & Chang MCY (2012) Identification and characterization of a multifunctional dye peroxidase from a lignin-reactive bacterium. *ACS Chem Biol* **7**, 2074–2081.

43 Ahmad M, Roberts JN, Hardiman EM, Singh R, Eltis LD & Bugg TDH (2011) Identification of DypB from *Rhodococcus jostii* RHA1 as a lignin peroxidase. *Biochemistry* **50**, 5096–5107.

44 Neet KE (1980) [7] Cooperativity in enzyme function: equilibrium and kinetic aspects. In Methods in Enzymology (Purich DL, ed.), pp. 139–192. Elsevier, Cambridge, MA.

45 Porter CM & Miller BG (2012) Cooperativity in monomeric enzymes with single ligand-binding sites. *Bioorganic Chem* **43**, 44–50.

46 Strittmatter E, Wachter S, Liers C, Ullrich R, Hofrichter M, Plattner DA & Piontek K (2013) Radical formation on a conserved tyrosine residue is crucial for DyP activity. *Arch Biochem Biophys* **537**, 161–167.

47 Linde D, Pogni R, Cañellas M, Lucas F, Guallar V, Baratto MC, Sinicropi A, Sáez-Jiménez V, Coscolín C, Romero A *et al.* (2015) Catalytic surface radical in dye-decolorizing peroxidase: a computational, spectroscopic and site-directed mutagenesis study. *Biochem J* **466**, 253–262.

48 Zitare UA, Szuster J, Scocozza MF, Espinoza-Cara A, Leguto AJ, Morgada MN, Vila AJ & Murgida DH (2019) The role of molecular crowding in long-range metalloprotein electron transfer: dissection into site- and scaffold-specific contributions. *Electrochim Acta* **294**, 117–125.

49 Zitare UA, Szuster J, Santalla MC, Morgada MN, Vila AJ & Murgida DH (2020) Dynamical effects in metalloprotein heterogeneous electron transfer. *Electrochim Acta* **342**, 136095.

50 Zitare UA, Szuster J, Santalla MC, Llases ME, Morgada MN, Vila AJ & Murgida DH (2019) Fine tuning of functional features of the Cu $_A$ site by loop-directed mutagenesis. *Inorg Chem* **58**, 2149–2157.

51 Oviedo-Rouco S, Perez-Bertoldi JM, Spedalieri C, Castro MA, Tomasina F, Tortora V, Radi R & Murgida DH (2020) Electron transfer and conformational transitions of cytochrome c are modulated by the same dynamical features. *Arch Biochem Biophys* **680**, 108243.

52 Fernández-Fueyo E, Davó-Siguero I, Almendral D, Linde D, Baratto MC, Pogni R, Romero A, Guallar V & Martínez AT (2018) Description of a non-canonical Mn(II)-oxidation site in peroxidases. *ACS Catal* **8**, 8386–8395.

53 Yoshida T, Ogola HJO, Amano Y, Hisabori T, Ashida H, Sawa Y, Tsuge H & Sugano Y (2016) *Anabaena* sp. DyP-type peroxidase is a tetramer consisting of two asymmetric dimers: structural study of AnaPX. *Proteins* **84**, 31–42.

54 Bendtsen J, Nielsen H, Widdick D, Palmer T & Brunak S (2005) Prediction of twin-arginine signal peptides. *BMC Bioinformatics* **6**, 167.

55 Berglund GI, Carlsson GH, Smith AT, Szöke H, Henriksen A & Hajdu J (2002) The catalytic pathway of horseradish peroxidase at high resolution. *Nature* **417**, 463–468.

56 Colpa DI, Fraaije MW & Groningen Rijksuniversiteit (2018) Exploring the biochemical and biocatalytic properties of bacterial DyP-type peroxidases. PhD Thesis, 127p.

57 Katoh K, Rozewicki J & Yamada KD (2019) MAFFT online service: multiple sequence alignment, interactive sequence choice and visualization. *Brief Bioinform* **20**, 1160–1166.

58 Darriba D, Taboada GL, Doallo R & Posada D (2011) ProtTest 3: fast selection of best-fit models of protein evolution. *Bioinformatics* **27**, 1164–1165.

59 Guindon S & Gascuel O (2003) A simple, fast, and accurate algorithm to estimate large phylogenies by maximum likelihood. *Syst Biol* **52**, 696–704.

60 Lemoine F, Domelevo Entfellner J-B, Wilkinson E, Correia D, Dávila Felipe M, De Oliveira T & Gascuel O (2018) Renewing Felsenstein's phylogenetic bootstrap in the era of big data. *Nature* **556**, 452–456.

61 Yang Z (2007) PAML 4: Phylogenetic Analysis by Maximum Likelihood. *Mol Biol Evol* **24**, 1586–1591.

62 Gasteiger E, Hoogland C, Gattiker A, Duvaud S, Wilkins MR, Appel RD & Bairoch A (2005) Protein identification and analysis tools on the ExPASy server. In The Proteomics Protocols Handbook (Walker JM, ed.), pp. 571–607. Humana Press, Totowa, NJ.

63 McCoy AJ, Grosse-Kunstleve RW, Adams PD, Winn MD, Storoni LC & Read RJ (2007) *Phaser* crystallographic software. *J Appl Crystallogr* **40**, 658–674.

64 Winn MD, Ballard CC, Cowtan KD, Dodson EJ, Emsley P, Evans PR, Keegan RM, Krissinel EB, Leslie AGW, McCoy A *et al.* (2011) Overview of the *CCP* 4 suite and current developments. *Acta Crystallogr D Biol Crystallogr* **67**, 235–242.

65 Murshudov GN, Skubák P, Lebedev AA, Pannu NS, Steiner RA, Nicholls RA, Winn MD, Long F & Vagin AA (2011) *REFMAC* 5 for the refinement of macromolecular crystal structures. *Acta Crystallogr D Biol Crystallogr* **67**, 355–367.

66 Emsley P, Lohkamp B, Scott WG & Cowtan K (2010) Features and development of *Coot*. *Acta Crystallogr D Biol Crystallogr* **66**, 486–501.

67 Winter G, Waterman DG, Parkhurst JM, Brewster AS, Gildea RJ, Gerstel M, Fuentes-Montero L, Vollmar M, Michels-Clark T, Young ID *et al.* (2018) *DIALS* : implementation and evaluation of a new integration package. *Acta Crystallogr D Struct Biol* **74**, 85–97.

68 Matthews BW (1968) Solvent content of protein crystals. *J Mol Biol* **33**, 491–497.

69 Joosten RP, Long F, Murshudov GN & Perrakis A (2014) The *PDB_REDO* server for macromolecular structure model optimization. *IUCrJ* **1**, 213–220.

70 Chen VB, Arendall WB, Headd JJ, Keedy DA, Immormino RM, Kapral GJ, Murray LW, Richardson JS & Richardson DC (2010) *MolProbity* : all-atom structure validation for macromolecular crystallography. *Acta Crystallogr D Biol Crystallogr* **66**, 12–21.

Supporting information

Additional supporting information may be found online in the Supporting Information section at the end of the article.

Fig. S1. Representation of the homology model.
Fig. S2. A multiple sequence alignment of the AncDyPD-b1 and three fungal DyPs.
Fig. S3. UV-Vis absorbance spectra.
Fig. S4. Activity vs. pH measured with two different dyes.
Fig. S5. AncAltDyPD-b1 kobs vs. substrate concentration.
Fig. S6. kobs vs. substrate concentration graphs.

Fig. S7. TatP 1.0 Server prediction.

Table S1. X-ray data collection and refinement statistics.

Table S2. Relative remaining activity of AncDyPD-b1 and AncAltDyPD-b1.

Table S3. Steady-state kinetic parameters of AncAlt-DyPD-b1.

Data S1. Primers used for protein variants generation.

Data S2. Steady-state kinetic models.

Data S3. Ancestral DyPs selected for experimental characterization.

Data S4. Sulfoxidation assay.